Geochemistry, Geophysics, Geosystems

RESEARCH ARTICLE
10.1029/2020GC008957

The Evolution of Seafloor Spreading Behind the Tip of the Westward Propagating Cocos-Nazca Spreading Center

Deborah K. Smith[1], Hans Schouten[2], Ross Parnell-Turner[3], Emily M. Klein[4], Johnson Cann[5], Charles Dunham[6], Gabriella Alodia[6], Iker Blasco[7], Benjamin Wernette[4], Dominik Zawadzki[8], Elvira Latypova[9], Sara Afshar[3], and Scott Curry[2]

[1]National Science Foundation, Alexandria, VA, USA, [2]Woods Hole Oceanographic Institution, Woods Hole, MA, USA, [3]Scripps Institution of Oceanography, University of California, San Diego, La Jolla, CA, USA, [4]Division of Earth and Ocean Sciences, Duke University, Durham, NC, USA, [5]School of Earth and Environment, University of Leeds, UK and Curlew Cottage, Penrith, UK, [6]School of Earth and Environment, University of Leeds, Leeds, UK, [7]Geological Survey of Spain, Instituto Geológico y Minero de España, Madrid, Spain, [8]Institute of Marine and Environmental Sciences, University of Szczecin, Szczecin, Poland, [9]Department of Regional Geology, Saint Petersburg State University, St Petersburg, Russia

Key Points:
- At the Galapagos triple junction rifting changes to full magmatic spreading in stages within the Cocos-Galapagos microplate spreading regime
- Magnetic anomalies and linear off-axis topography show magmatic spreading developed rapidly when opening was between Cocos and Nazca plates
- Initial segment lengths at the tip of the Galapagos gore appear constant at ~20 km, but segment lengths are larger farther from the tip

Correspondence to:
D. K. Smith,
dksmith@nsf.gov

Citation:
Smith, D. K., Schouten, H., Parnell-Turner, R., Klein, E. M., Cann, J., Dunham, C., et al. (2020). The evolution of seafloor spreading behind the tip of the westward propagating Cocos-Nazca spreading center. *Geochemistry, Geophysics, Geosystems*, *21*, e2020GC008957. https://doi.org/10.1029/2020GC008957

Received 3 FEB 2020
Accepted 6 MAY 2020
Accepted article online 11 MAY 2020

Abstract At the Galapagos triple junction in the equatorial Pacific Ocean, the Cocos-Nazca spreading center does not meet the East Pacific Rise (EPR) but, instead, rifts into 0.4 Myr-old lithosphere on the EPR flank. Westward propagation of Cocos-Nazca spreading forms the V-shaped Galapagos gore. Since ~1.4 Ma, opening at the active gore tip has been within the Cocos-Galapagos microplate spreading regime. In this paper, bathymetry, magnetic, and gravity data collected over the first 400 km east of the gore tip are used to examine rifting of young lithosphere and transition to magmatic spreading segments. From inception, the axis shows structural segmentation consisting of rifted basins whose bounding faults eventually mark the gore edges. Rifting progresses to magmatic spreading over the first three segments (s1–s3), which open between Cocos-Galapagos microplate at the presently slow rates of ~19–29 mm/year. Segments s4–s9 originated in the faster-spreading (~48 mm/year) Cocos-Nazca regime, and well-defined magnetic anomalies and abyssal hill fabric close to the gore edges show the transition to full magmatic spreading was more rapid than at present time. Magnetic lineations show a 20% increase in the Cocos-Nazca spreading rate after 1.1 Ma. The near-axis Mantle Bouguer gravity anomaly decreases eastward and becomes more circular, suggesting mantle upwelling, increasing temperatures, and perhaps progression to a developed melt supply beneath segments. Westward propagation of individual Cocos-Nazca segments is common with rates ranging between 12 and 54 mm/year. Segment lengths and lateral offsets between segments increase, in general, with distance from the tip of the gore.

Plain Language Summary A fundamental question in the study of mid-ocean ridges is how spreading centers initiate and change through time. At the Galapagos triple junction in the equatorial Pacific, the oceanic crust is being broken apart to form rift basins, which develop into individual mid-ocean ridge spreading segments. Bathymetry, magnetic, and gravity data were collected to help understand the stages in the transition from rift basins to a magmatic seafloor spreading center. From inception, the developing spreading center is composed of individual segments that are offset from each other. Currently, rifting progresses to magmatic spreading over three segments, which opened at slow spreading rates. Older spreading segments originated at faster-spreading rates. Data indicate that the change from rifting to full magmatic spreading was more rapid in these older segments. Near the spreading axis, gravity data show that temperatures increase beneath segments as they mature, suggesting that magma supply is developing beneath the segments. Propagation of the western ends of segments is common. Understanding how seafloor spreading initiates and forms a segmented mid-ocean ridge provides information on how mantle melting is established beneath a rift zone and how tectonic plate boundaries evolve.

1. Introduction

At the Galapagos triple junction, the Cocos, Nazca, and Pacific plates meet and surround the Galapagos microplate (Figure 1). The westward propagation of the Cocos-Nazca (C-N) spreading center has produced a V-shaped topographic gore (Galapagos gore; Holden & Dietz, 1972) with its present apex located ~25 km

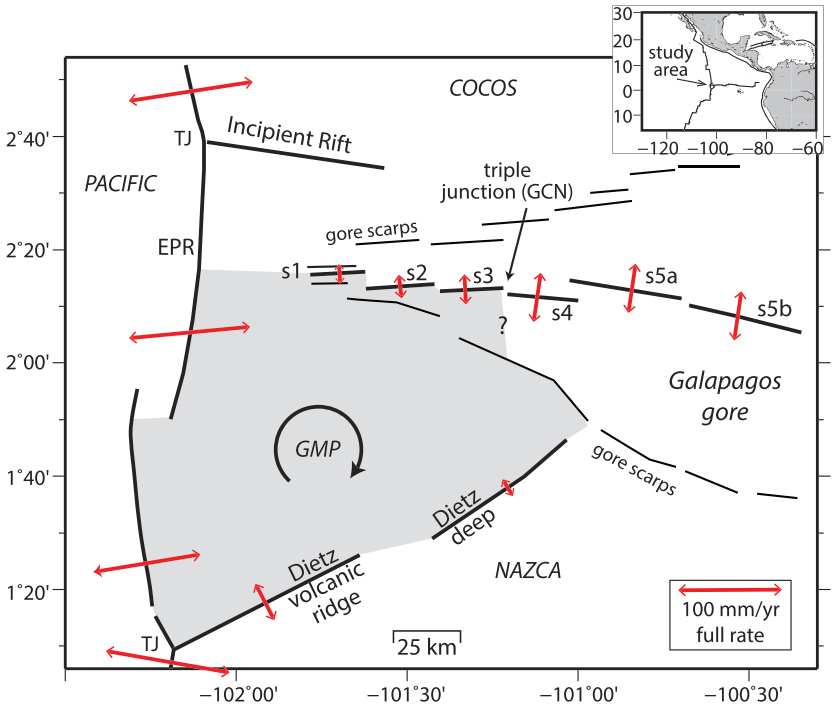

Figure 1. Schematic showing the different spreading regimes around the Galapagos microplate (GMP) at the Galapagos triple junction (modified from Smith & Schouten, 2018, using C-N opening rates from this study). Red arrows: spreading directions scaled by spreading rate. TJ = triple junction. EPR = East Pacific Rise. Faults bounding the Galapagos gore are shown. Segments within the gore are labeled. Also marked is the probable location of the Galapagos-Cocos-Nazca (GCN) TJ.

from the axis of the East Pacific Rise (EPR), widening to the east as a result of spreading between the Cocos and Nazca plates. At the western end of the gore, oceanic lithosphere that was accreted on the east flank of the EPR near 2°15′N (Lonsdale, 1988) is being rifted apart. Over the past 5 Ma, the tip of this rifting has not reached the EPR to form a true ridge-ridge-ridge triple junction but rather has remained at distances of 20–50 km from the EPR axis (Schouten et al., 2008) rifting into 0.3–0.75 Ma crust.

North and south of the gore tip, two secondary rifts do link with the EPR each forming a true ridge-ridge-ridge triple junction (Figure 1). To the north, Incipient Rift meets the EPR at 2°40′N to form the northern triple junction. In the south at 1°10′N, Dietz volcanic ridge meets the EPR and presently forms the southern boundary of the Galapagos microplate, which was formed ~1.4 Ma (Klein et al., 2005; Lonsdale, 1988; Lonsdale et al., 1992; Schouten et al., 2008; Smith et al., 2011, 2013). Since 1.4 Ma, opening at the tip of the gore has been within the very slow spreading Cocos-Galapagos (C-G) microplate regime.

The western end of the Galapagos gore contains a chain of rift basins that shows the current progressive breakup of the oceanic lithosphere and the establishment of magmatic seafloor spreading segments. Using newly collected bathymetry, magnetic, and gravity data, we examine the formation and evolution of the first nine segments extending ~400 km east from the gore tip near 101°48′W (Figures 2 and 3). We find that the current rift-to-spreading transition occurs ~60–70 km from the gore tip. Volcanic features first appear within the rift basins ~25 km from the tip. Initial segment lengths and offsets change as segments mature. Understanding how seafloor spreading initiates and forms a segmented mid-ocean ridge provides information on how mantle upwelling is established beneath a rift and how plate boundaries evolve.

2. Previous Studies

Based on bathymetry data available at the time, Lonsdale (1977) suggested that seafloor spreading in the western section of the Galapagos gore begins within Hess Deep rift (referred to here as Segment s2).

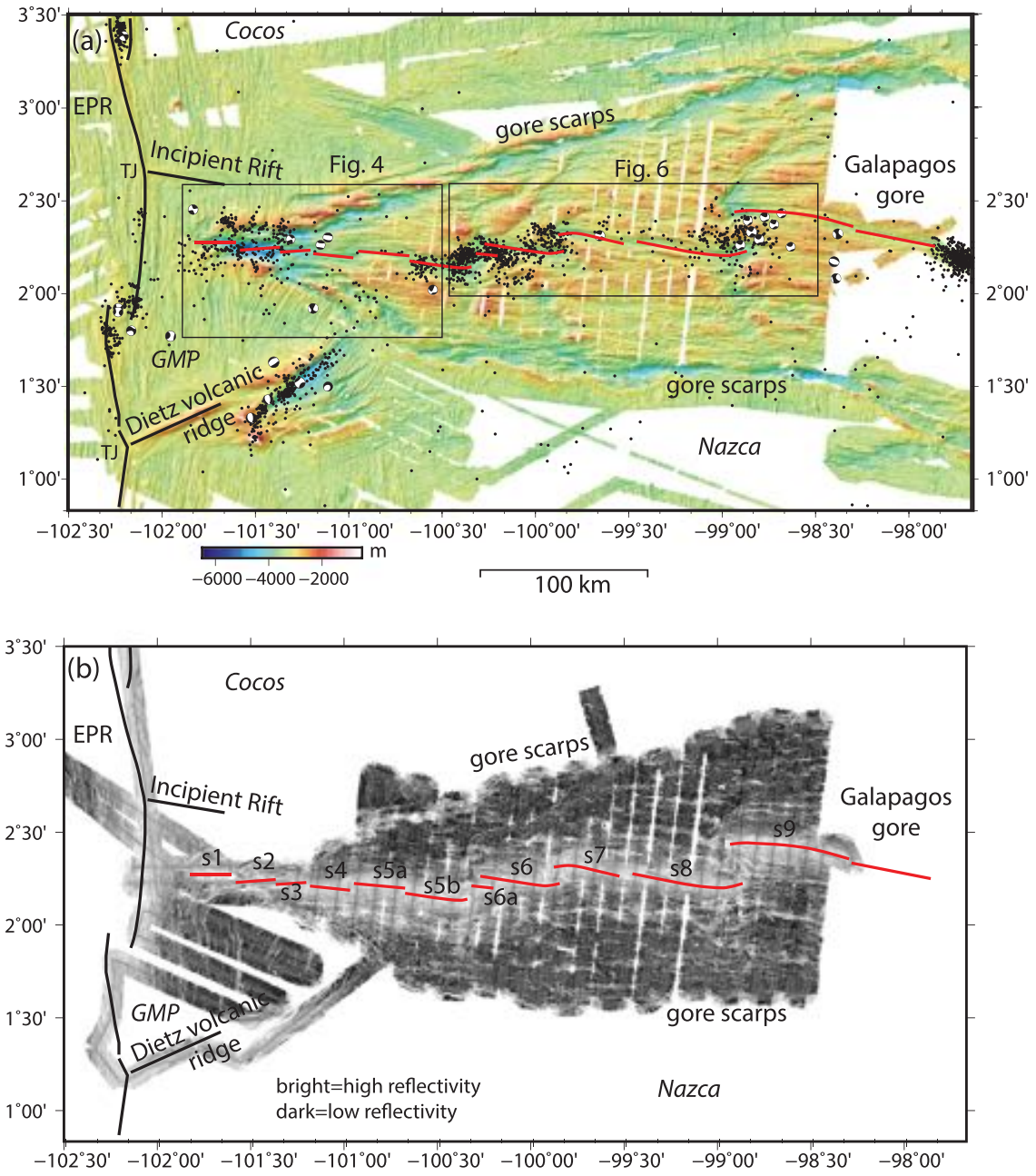

Figure 2. (a) Bathymetry of the Galapagos triple junction region with hydrophone (black dots) and teleseismically recorded seismicity (circles with focal mechanisms) (Ekström et al., 2012; Fox et al., 2001). Solid black lines: plate boundaries including Incipient Rift. Red lines: spreading segments. Areas shown in Figures 4 and 6 are outlined. TJ = triple junction. (b) Seafloor backscatter from the EM122 bathymetry. Segments are numbered from the western tip of the gore. Other labels are the same as in (a). Bright shades: high reflectivity, generally associated with exposed rock or steep gradients. Dark shades: low reflectivity, generally associated with significant sediment cover.

Searle and Francheteau (1986) concluded from patterns observed in GLORIA side scan sonar data that the current active tip of rifting is located at the western end of Hess Deep rift. They also noted, however, the existence of a basin located to the west and a few km north of Hess Deep rift, which they suggested could be a possible extension of the rift tip. Searle (1989) combined GLORIA side scan data with magnetic anomaly data from Hey (1977) to identify and describe the general morphology of the spreading axis within the gore west of 95.5°W. Lonsdale (1988) examined the configuration and evolution of the major

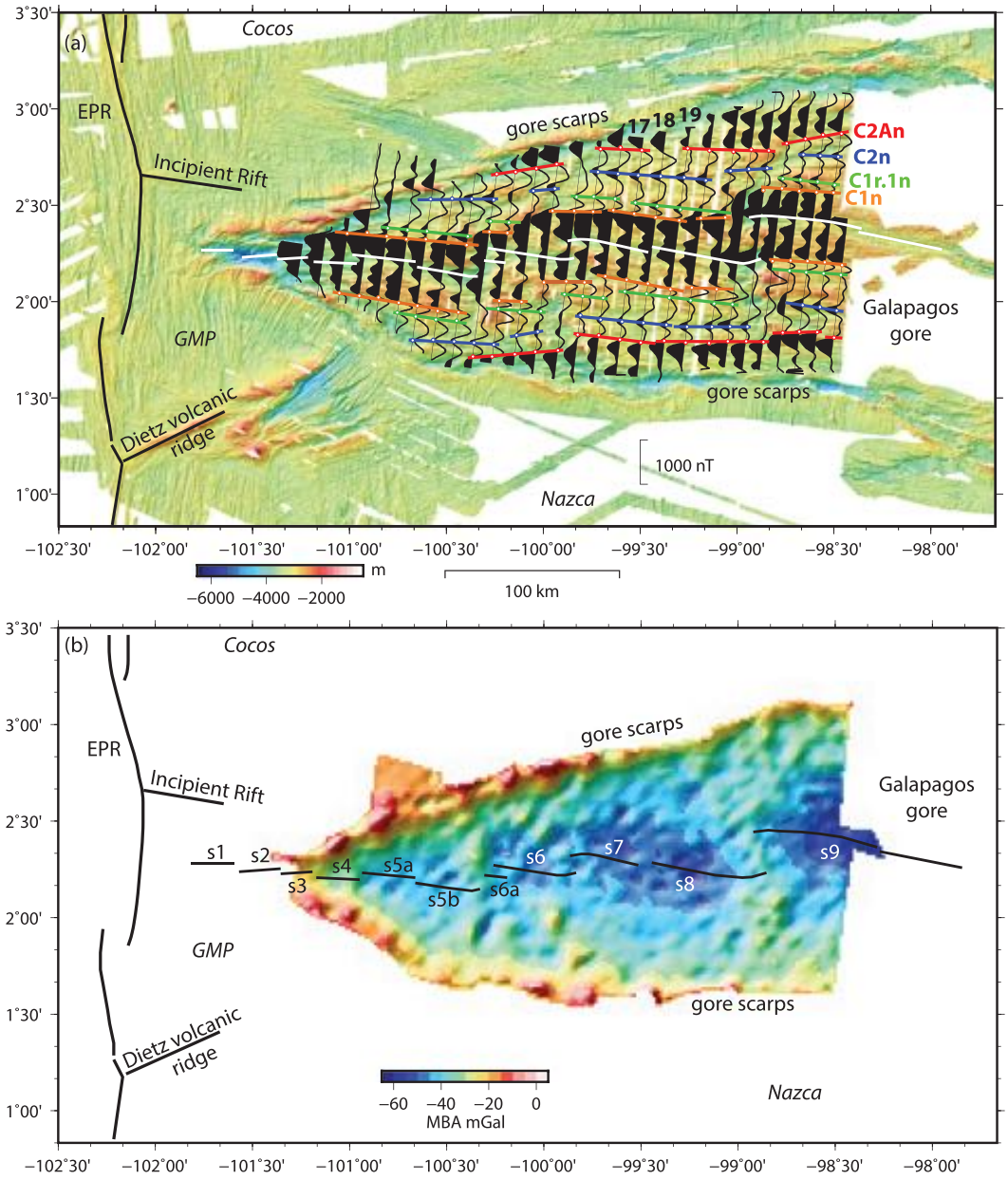

Figure 3. (a) Magnetic data plotted along ship tracks. Labels as in Figure 1. Colored lines: magnetic anomalies. Anomalies are well resolved and correlated along-axis except where disrupted by the traces of segment offsets. Numbered profiles (17–19) are displayed in Figure 8. (b) Mantle Bouguer gravity anomaly. Near-axis values decrease toward the east and become more centered under the axis.

plate boundaries in the triple junction region and, in particular, how the westward propagation of the spreading axis has varied through time.

Since these early tectonic studies, the western end of the Galapagos gore has been the focus of numerous efforts, including Ocean Drilling Project (ODP) Leg 147 and Integrated Ocean Drilling Program (IODP) Leg 345, which drilled the Intrarift Ridge (IRR) in Hess Deep rift (e.g., Ferrini et al., 2013; Francheteau et al., 1990; Gillis et al., 1993, 2014; Karson et al., 2002; MacLeod et al., 1996; Stewart et al., 2003). The IRR has been interpreted as a south facing, low-angle, long-lived normal fault (i.e., detachment fault) (e.g., Ballu et al., 1999; Francheteau et al., 1990; Lonsdale, 1988; Smith & Schouten, 2018; Wiggins et al., 1996), and studies have been conducted primarily to explore the geochemistry and architecture of the crust and upper mantle exposed at the seafloor.

Smith and Schouten (2018) examined the three initial rift basins developing in the Galapagos gore and suggested that the basin identified by Searle and Francheteau (1986) west of Hess Deep rift represents the earliest stage of rifting (s1, Figure 2a). The next segment to the east, the 24-km-long Hess Deep rift (s2), was identified as a transitional segment from rifting to magmatic seafloor spreading, displaying the growth of an axial volcanic ridge (AVR) in its eastern section and flanked on the north by an active low-angle detachment fault (the IRR). The IRR is the only active detachment fault that Smith and Schouten (2018) could identify along the base of the gore scarps from the existing data, and they suggested that IRR formation was in response to a slow-down in spreading rate and presumed lower melt supply, resulting from the formation of the Galapagos microplate. Smith and Schouten (2018) concluded that full magmatic spreading (i.e., along the entire length of a segment) currently begins at Segment s3.

The pattern of hydrophone-detected T-phase origins and teleseismically recorded seismicity in the Galapagos triple junction region (Ekström et al., 2012; Fox et al., 2001) was used to support the interpretation of full magmatic spreading at Segment s3 (Figure 2a). Deformation (defined by earthquake locations) is distributed broadly at the tip of the gore, occurring along the initial gore scarps as well as subsequent faults bounding the rift axis. The broad zone of deformation continues from west of s1 to the start of s3. East of this point, earthquakes are located primarily at the rift axis. Smith and Schouten (2018) inferred that magma is present in an adequate quantity beneath the axis of s3 to accommodate full magmatic spreading and, thus, there is not sufficient stress to cause continued slip on the gore border faults.

Smith and Schouten (2018) noted that the axes of s2 and s3 trend ~087 (the trend of s1 is poorly constrained), which suggests s2 and s3 open within the C-G spreading regime (Figure 1). Starting at ~101°10′W (s4), however, the segment axes trend roughly 099, which is similar to that given by plate model NUVEL 1A (097) for an orthogonal segment opening between the Cocos and Nazca plates (DeMets et al., 1994). Smith and Schouten (2018) associated the initiation of C-G spreading at ~1.4 Ma with a slowdown in spreading rate at the gore tip. They suggested that before 1.4 Ma, opening was between the Cocos and Nazca plates at an intermediate spreading rate of ~40 mm/year (from plate model NUVEL 1A) all the way to the rift tip. After that, formation of s1, s2, and s3 occurred as part of the new plate kinematic system opening between Cocos and the Galapagos microplate. Smith and Schouten (2018) used the C-N spreading rate of 40 mm/year to estimate the current spreading rates of s1, s2, and s3 to be ~16, ~19, and ~24 mm/year, respectively.

3. Data

Prior to this study, multibeam bathymetry data were sufficient to define the general characteristics of the first four rift segments (s1–s4) at the western end of the Galapagos gore (Smith & Schouten, 2018). However, data coverage east of ~101°W was limited to a single swath of bathymetry data collected over the axis of s5–s8 during a transit of the NOAA ship *Okeanos Explorer* in 2011 (cruise EX1103; https://oceanexplorer.noaa.gov/okeanos/explorations/ex1103/welcome.html). No multibeam bathymetry data were available over the western half of s9, and off-axis data for Segments s3–s9 were sparse. In April–May 2018 aboard R/V *Sally Ride* (Leg 1806), bathymetry, magnetic, and gravity data were collected over the axial zone of the first nine segments within the Galapagos gore and off-axis to their points of initiation at the north and south scarps of the gore. Bathymetry data were acquired using a Kongsberg EM122 multibeam echosounder and logged with Kongsberg SIS software (Seafloor Information System, v 4.3.2). Survey lines were run at a vessel speed of 10.5~kt (~5.4 m/s), on average. Most of the survey was conducted on NNE-SSW tracks with ~10 km spacing between ship tracks to provide almost 100% bathymetric coverage (Figure 2a). Sippican expendable bathythermograph (XBT) drops were used to calculate sound velocity profiles for input to the EM122 and were generally taken every day when collecting EM122 data. The raw EM122 data were gridded using MB-System software (Caress & Chayes, 1996), and both bathymetry and derived seafloor backscatter netcdf files were generated. The seafloor backscatter derived from the EM122 system is shown in Figure 2b.

The magnetic field was measured with a SeaSPY magnetometer, with data logged using Marine Magnetics BOB software. The magnetometer was towed at full survey speed (~10.5 kt), and the towing cable length ranged between 233 and 300 m depending on the behavior of the cable during deployments. The magnetic data were merged with the vessel GPS feed and the position of the magnetometer interpolated relative to the ship. The magnetic anomalies along each track line (Figure 3a) were obtained by removing the International Geomagnetic Reference Field (IAGA, 2010) updated in 2015 from the total field data.

Gravity data were collected with a Bell Aerospace BGM-3 gravimeter. A gravity tie was obtained in San Diego, CA before the ship departed and upon arrival back in San Diego, CA. After applying a 360-s Gaussian filter and Eötvös correction, the free-air anomaly (FAA) was calculated by subtracting observed values from the International Gravity Formula 1980. The mantle Bouguer anomaly (MBA) was calculated by removing the gravitational effects of the water-crust and crust mantle interfaces using an upward-continuation method assuming a crustal thickness of 6 km (Parker, 1972). The resulting MBA map (Figure 3b) primarily reflects variations in mantle thermal structure and variations in the thickness and/or density of the crust (Kuo & Forsyth, 1988; Lin et al., 1990). The following parameters were used in the calculation of the MBA: crustal thickness of 6 km; crustal density of 2,700 kg/m^3; and mantle density of 3,300 kg/m^3. A thermal correction to account for the gravitational effects of upwelling and cooling of mantle material was not applied to the MBA. Modeling the thermal correction in this complex tectonic setting will be completed in the future.

Dredging was a significant component of the operations at sea, and rock samples were collected during 63 successful dredges along the axes of Segments s2–s9 and adjacent features. Results of the geochemical analyses will be presented in forthcoming papers.

4. Characteristics of Segments s1–s9

4.1. Axial Morphology

The bathymetry data in combination with seafloor reflectance and topographic slopes were used to examine the detailed characteristics of the basins that are the current locus of rifting and the transition to seafloor spreading (s1–s3) as well as those to the east (s4–s9). The descriptions, interpretations, and spreading rates (discussed in a following section) of s1–s3 presented by Smith and Schouten (2018) have been re-evaluated and refined with the new information available from this study.

We interpret the ~17-km-long, ~6-km-wide, extensional basin at the western end of the Galapagos gore, first identified by Searle and Francheteau (1986), as representing the earliest stage of rifting (s1; Figures 4a and 4b). The current bounding faults of s1 have relief of ~0.7–1 km. The relief on these faults presumably will increase with continuing extension to match the relief (~2 km) on many of the northern gore bounding faults to the east. In detail, s1 is composed of deeps, whose maximum depth is ~4,400 m, and highs oriented in an approximate northeast/southwest direction. Similar northeast/southwest bathymetric trends are present south of the rift on the Galapagos microplate. As rifting continues, we assume s1 will become a single rift basin oriented normal to the C-G spreading direction. Lonsdale (1988) suggested there might be volcanic relief within this rift basin, but our new bathymetry data show no evidence of volcanic topography within the s1 basin.

Segment s2 is east of s1 and offset 3 km south. It is ~24 km long and ~15 km wide and displays significant changes in morphology along its axis. A deep basin in the western section of the rift (Hess Deep) has water depths exceeding 5,400 m, about 1 km deeper than observed in s1. Hummocky seafloor in its deep western section suggests volcanic topography as proposed by Lonsdale (1988), and basalts have been sampled as far west as ~101°30′W (e.g., Ferrini et al., 2013; Gillis et al., 2014). In the eastern section of s2, water depths shallow from ~4,900 to ~4,100 m from west to east along an AVR, which is ~12 km long and 4–6 km wide. The AVR reaches up to several hundred meters in relief, increasing in relief to the east. The flanks and top of the AVR are covered with small volcanic hummocks, and its morphology is similar to AVRs described at the slow spreading (~25 mm/year, full rate) northern Mid-Atlantic Ridge (MAR) (e.g., Searle et al., 2010). The s2 AVR appears to continue into s3 as described below.

The IRR borders s2 on the north and extends the length of the segment (Figure 4a). We interpret the IRR as an active detachment fault as did Smith and Schouten (2018) and others before them (e.g., Ballu et al., 1999; Francheteau et al., 1990; Lonsdale, 1988; Wiggins et al., 1996). Studies of oceanic detachment faults along slower spreading ridges suggest that magma supply plays an important role in the initiation and maintenance of slip on these faults (e.g., Buck et al., 2005; Olive et al., 2010; Tucholke et al., 2008; Whitney et al., 2013). At the Woodlark Basin in the southwest Pacific Ocean where continental crust is being rifted apart, it has been proposed that detachment fault formation signals the input of magma into an area (e.g., Hill et al., 1995; Little et al., 2007; Martínez et al., 2001; Taylor et al., 1999). Based on these studies, we

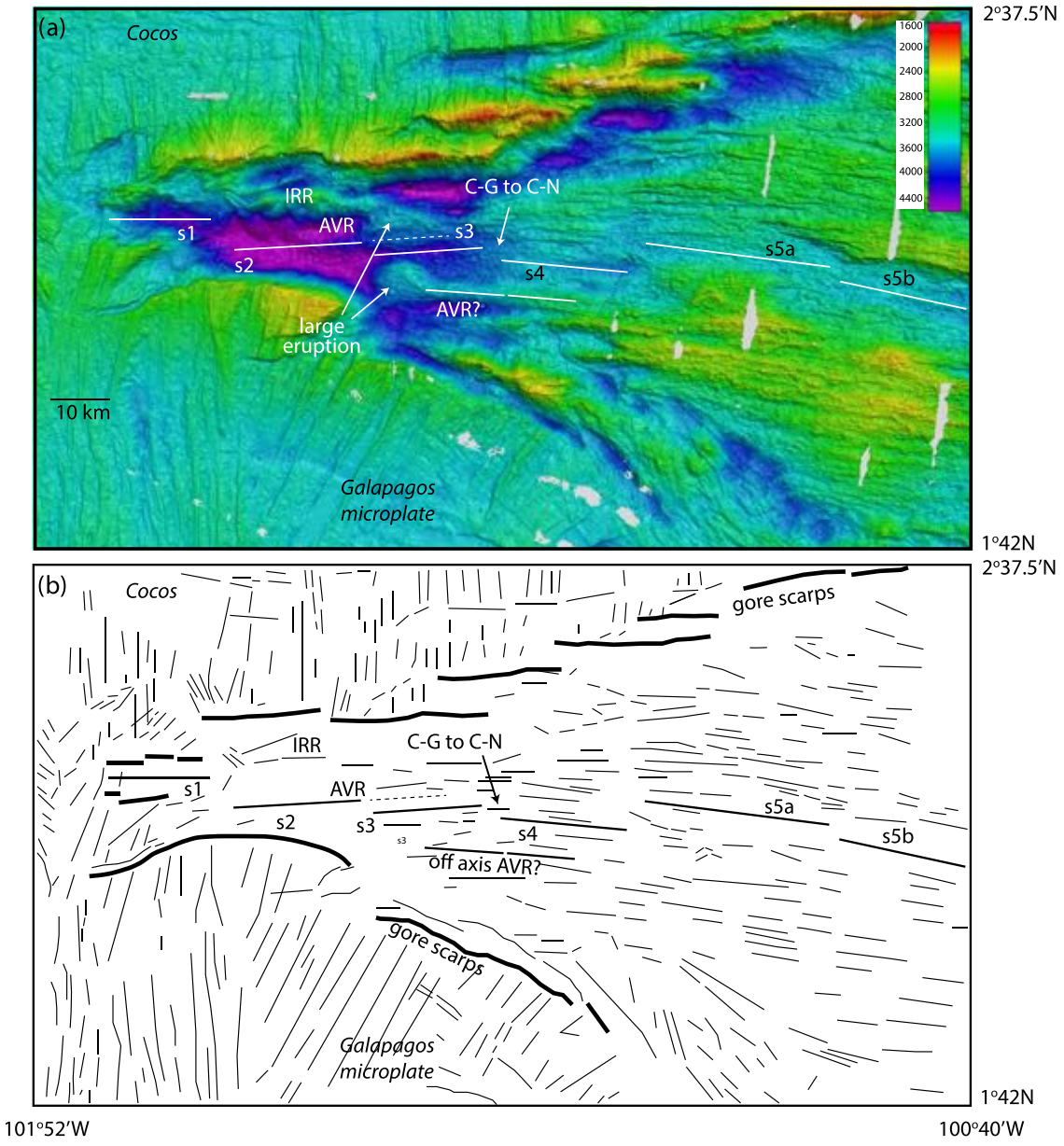

Figure 4. (a) Bathymetry within the box marked on Figure 2a showing segments at the western tip of the Galapagos gore. The location of the change in spreading regime from C-N to C-G occurs in the region marked. This is also the probable location of the GNC triple junction. Note the large pile of volcanics at the western end of s3. Solid white lines: segments. IRR = Intrarift Ridge; AVR = axial volcanic ridge. Dashed white line: possible continuation of the s2 AVR into s3. (b) Lineation map. Lines identified by eye from the map in (a). Thick black lines: gore scarps. Off-axis lineations show a change in the strike of the faults between s3 and s4.

conclude magma is being supplied along the length of s2. Magma may move laterally into s2 from the adjacent magmatic segment (s3), vertically from beneath the segment, or both, and is sufficient to produce voluminous flows along its eastern section to build the AVR.

The next segment east, s3, is ~18 km long and offset south of s2 by about 1.2 km. Prior to this study, there were significant gaps in the bathymetric coverage of s3. The new bathymetry data reveal the complete axial zone and off-axis topography. At the western end of s3, a large volume of lava erupted in the past. The lavas have been cut by axis-facing normal faults and spread off axis (Figure 4a). The current axis in the western part of s3 runs along a 2 km wide deep, which contains small volcanic cones. A volcanic ridge cut by

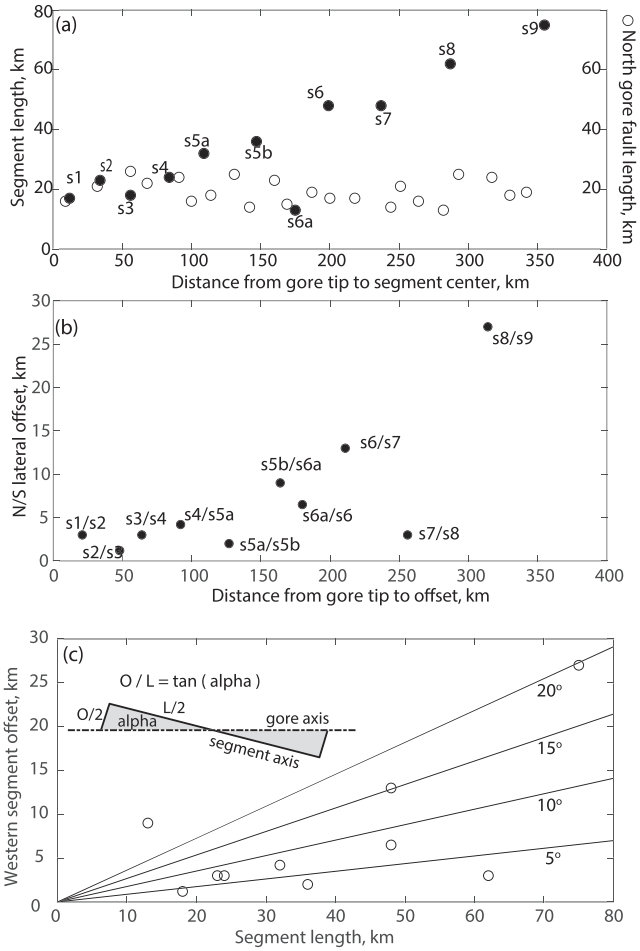

Figure 5. (a) Segment and gore fault lengths plotted as a function of distance from the gore tip. Filled black circles: segment lengths Open circles: lengths of faults bounding the gore on its northern side. Segment lengths increase, but fault lengths do not increase with distance from the gore tip. (b) Lateral offsets between segments measured in a north-south direction plotted as a function of distance to the gore tip. (c) Offset plotted versus segment length. Inset in upper left shows that if spreading direction is not orthogonal to the axis of the gore, segment offsets will increase with segment length. Alpha = angle between the gore axis and segment strike. L = segment length. O = segment offset. In the study area, C-N gore axis is ~088 and C-N segments are ~097 predicting an alpha of 9°. Lines: O/L for differing values of alpha.

small normal faults borders the deep on the north and appears to be the eastern continuation of the AVR in s2. Water depths shallow by about 300 m from west to east along the section of the volcanic ridge in s3. An analogous feature may be present ~65 km south of the s3 axis where a large (~500 m in relief) volcanic ridge appears to form the continuation of an off-axis ridge south of the s4 axis (Figure 4a). Volcanic ridges that straddle two segments may document the westward movement of magmatism into a developing segment.

The morphology of the eastern end of s3 is different from that of its western end (Figure 4a). The well-defined 2-km-wide axial deep in the western section disappears in the eastern half of the segment, the relief on the axis-facing faults decreases, and the axial volcanic topography looks similar to segments farther east. The change from C-G to C-N spreading occurs in this region, and the location of the Cocos-Nazca-Galapagos triple junction is probably here as well. Where exactly the change from slow spreading C-G to intermediate-spreading C-N occurs is hard to pinpoint based on the bathymetry data alone. The average strike of abyssal hill faults in the C-G spreading regime is 087 while their average strike is 097 in the C-N spreading regime. Based on the orientation of the abyssal hills, the transition between these spreading regimes occurs in the region near 101°10′W (Figure 4b).

The length of s4 is ~24 km. It is offset south of s3 by ~3 km. A volcanic mound has been constructed near the western end of s4, but east of this, the axis is defined by a shallow graben a few hundreds of meters deep and roughly 3 km wide. Isolated volcanic features cover the valley floor. Water depths in s4 average ~3,700 m compared to those in s3, which average ~4,200 m along the axial deep.

East of Segment s4 (Segments s5–s9), with the exception of a short segment identified between s5b and s6, the morphology of the axis is also that of a shallow graben with varying widths ranging up to 9 km. The grabens contain volcanic features that in some places string together to form a volcanic ridge a few tens of km in length and 100–200 m in relief. There are no features equivalent to the large AVR in s2. Additionally, no detachment faults are identified at the current spreading axis east of s2, which contains the IRR.

The MBA of the Galapagos gore is shown in Figure 3b. Within the gore, the data are not of sufficient resolution to be useful west of s5a. In general, though, the MBA values decrease to the east along the axis, suggesting hotter temperatures and increasing mantle upwelling beneath the segments. The first occurrence of a (somewhat diffuse) MBA low centered on the axis is ~180 km from the gore tip and is associated with s6. The MBA low becomes more circular and centered within individual segments farther east.

4.2. Segment Lengths and Offsets

In general, segment length increases as distance from the gore tip increases (Figure 5a). In contrast, lengths of faults bounding the gore on its northern side (also shown on Figure 5a) do not vary significantly with distance from the tip, and average 19 ± 4 km. If gore wall fault lengths reflect initial rift basin lengths, then initial segment lengths at the tip of the gore have been more or less constant at ~20 km for the last 5–6 Ma.

On average, north-south lateral offsets are larger at greater distances from the gore tip with the offset between s8 and s9 being notably large (>25 km; Figure 5b). Westward propagation of segments can increase lateral offset by eliminating segments. As an example, the very short segment s6a is being overtaken by the westward propagation of s6. If s6a is eliminated, the lateral offset between s5b and s6 will become ~18 km,

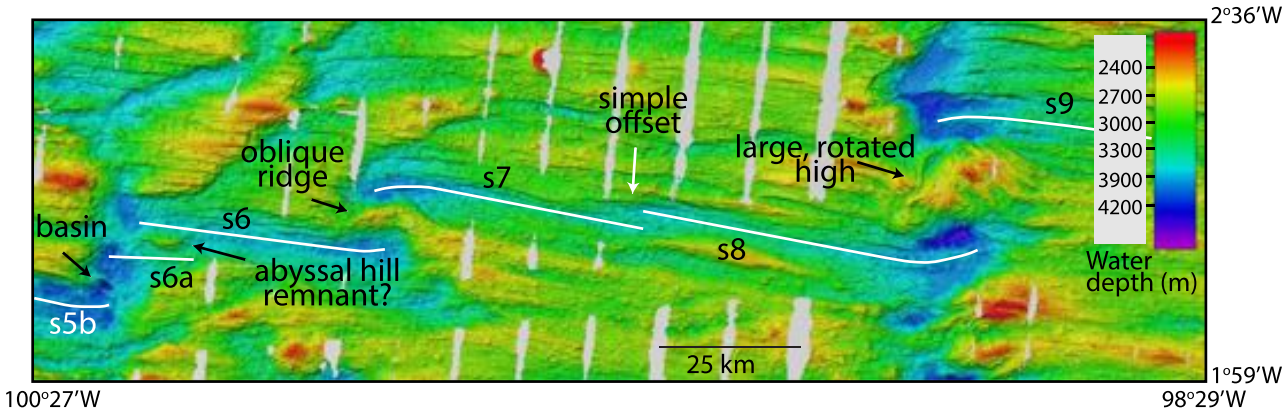

Figure 6. Bathymetry within the box indicated on Figure 2b. White lines: spreading segments. The styles of offset between segments are labeled.

which would be larger than all other offsets except for the one between s8 and s9 (Figure 5b). North-south lateral offset also could be a function of segment length (Figure 5c). Because the C-N spreading direction (~007) is not orthogonal to the gore symmetry axis (~088), offsets between longer segments will be larger (Figure 5c, inset).

The offsets between s1, s2, s3, and s4 are simple offsets of less than 3 km with no defining topographic features within them (Figure 4a). Starting at s4, however, different styles of offset are observed (Figure 6) and described below. A topographic ridge, ~1 km wide, 100 m high, and oriented at high angle to the overall ridge axis trend, separates s4 and s5a. Within the offset of s5b and s6a is a 600-m-deep basin flanked on the north and south by ridges oriented oblique to spreading. To the east, it appears that a recent and rapid episode of westward propagation of s6 has broken into abyssal hill topography and isolated a small (~7-km-long) section of the topography that now bounds s6a on the north from s6. Farther east, a large topographic ridge separates s6 and s7. The ridge is ~7 km wide and 1 km in relief. Finally, the offset between s7 and s8 is simple and just a few km wide, but the next offset east is very large. The ~27-km-wide lateral offset between s8 and s9 contains a semicircular topographic high that is ~17 km in width in the north-south direction and over 1 km high. It is faulted and rotated.

5. Off-Axis Topography and Magnetic Data (s4–s9)

The off-axis topography of the segments that are magmatically spreading and opening between Cocos and Nazca (s4–s9) displays a well-defined, linear, faulted abyssal hill fabric. The tops and outward facing slopes of the abyssal hills are coated with abundant volcanic cones. The magnetic isochrons that record magmatic spreading are well behaved from the early Bruhnes through anomaly C2An (Figure 3a). The anomalies are clearly recognizable, and individual anomalies can be correlated along axis until interrupted by the off-axis traces of segment propagation. Well-defined magnetic anomalies and linear, faulted off-axis seafloor topography close to the gore scarps suggest that normal magmatic spreading begins soon after rifting.

Three profiles that are unaffected by rift propagation were selected for magnetic data analysis (labeled 17–19 on Figure 3a). In Figure 7a, total distance between picked magnetic chrons is plotted versus time for the three profiles, and spreading rates are estimated using a linear fit. An increase in spreading rate is evident at ~1.1 Ma. Prior to that time, the opening rate between C-N was 39 mm/year, and since then, it has been 48.2 mm/year. The opening rate of 48.2 mm/year is larger than the value of 40 mm/year obtained from plate model NUVEL 1A (DeMets et al., 1994) and more consistent with the value of 47 mm/year obtained from plate model MORVEL for current plate motions (DeMets et al., 2010). We note, though, that the NUVEL 1A spreading direction of 007 is more consistent with the average strike of C-N spreading segments and seafloor fabric than the 003 spreading direction obtained from MORVEL. Our results support the conclusions of Wilson and Hey (1995), who identified a similar spreading rate change near 1.5 Ma. We have found no indication of the change in the seafloor topography, however.

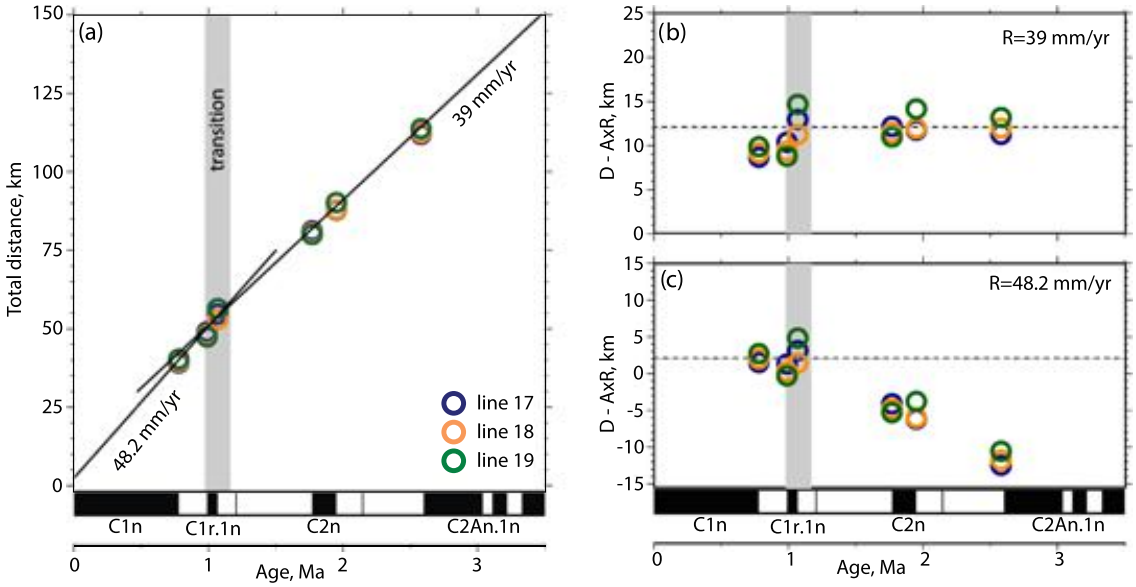

Figure 7. Estimates of Cocos-Nazca plate separation rates. Blue/orange/green circles: magnetic chron picks from Lines 17–19, respectively (line locations marked on Figure 3a). (a) Full spreading rate distance versus age. Black lines: best fitting linear trends with full spreading rates noted, obtained independently for picks before and after C1r.1n.o. Gray band: transition between two apparent spreading rates at ~1.1 Ma. (b) Reduced spreading distance versus age for picks before C1r.1n.o. Reduced distance is defined as the full spreading rate distance (D) minus the product of the age and the reduction rate (AxR) determined from the best fitting line in (a) (DeMets & Wilson, 2008). A change in spreading rate is indicated at ~1.1 Ma. (c) Reduced spreading distance versus age for picks after C1r.1n.o. The nonzero intercept suggests an ~2 km outward displacement of the magnetic polarity transition zones of Anomaly 1 from its modeled position.

DeMets and Wilson (2008) documented the displacement of magnetic polarity transition zones away from the axis from their idealized positions and suggested this could be caused by several processes including off-axis diking, eruption or flow of lavas off-axis, and the addition of magnetized gabbros at the base of the crust. To assess outward shift of recent magnetic polarity transition zones in the study area and possibly place constraints on these processes, we show rate reduced plots in Figures 7b and 7c. Reduced distance is obtained by subtracting the product of the age and spreading rate from the total spreading rate distance (DeMets & Wilson, 2008). The dashed line in Figure 7b represents a constant spreading rate of 39 mm/year; the best fitting rate for ages >1.1 Ma (Figure 7a) and clearly shows a spreading rate change at ~1.1 Ma. The dashed line in Figure 7c represents a constant spreading rate of 48.2 mm/year, the best fitting rate for ages <1.1 Ma. The nonzero, positive y intercept of this line (Figures 7a and 7c) implies an outward displacement of the magnetic polarity transition zones of magnetic chron C1n of ~2 km. The global average reported by DeMets and Wilson (2008) also is ~2 km, suggesting the characteristics of the magnetic source layer at this section of the C-N spreading center are similar to other mid-ocean ridges. Whether the outward displacement varies along the C-N axis remains unclear.

Synthetic magnetic anomalies were calculated for the three profiles using the program MODMAG (Mendel et al., 2005), assuming a magnetized layer of thickness 0.5 km, accounting for the transition zone between adjacent inversely magnetized blocks using a contamination coefficient of 0.9 (Tisseau & Patriat, 1981). Blocks in the model were assumed to have acquired magnetization at a latitude of 2°N, in a north-south orientation. Adjustments to spreading rate and spreading asymmetry were made to minimize the residual between observed and modeled anomalies (Figure 8), resulting in good fits for chrons C1n to C2An. In the model between 0 and 1 Ma, a total spreading rate of ~48.2 mm/year is used, and between 1 and 4 Ma, we use 39 mm/year, with modest asymmetry ranging from 3–10%.

6. Discussion

6.1. Comparison of Two Spreading Regimes

A change in spreading regime occurred ~1.4 Ma with the isolation of the Galapagos microplate. Its possible effect on the transition to magmatic seafloor spreading is considered below. Figure 1 shows the current

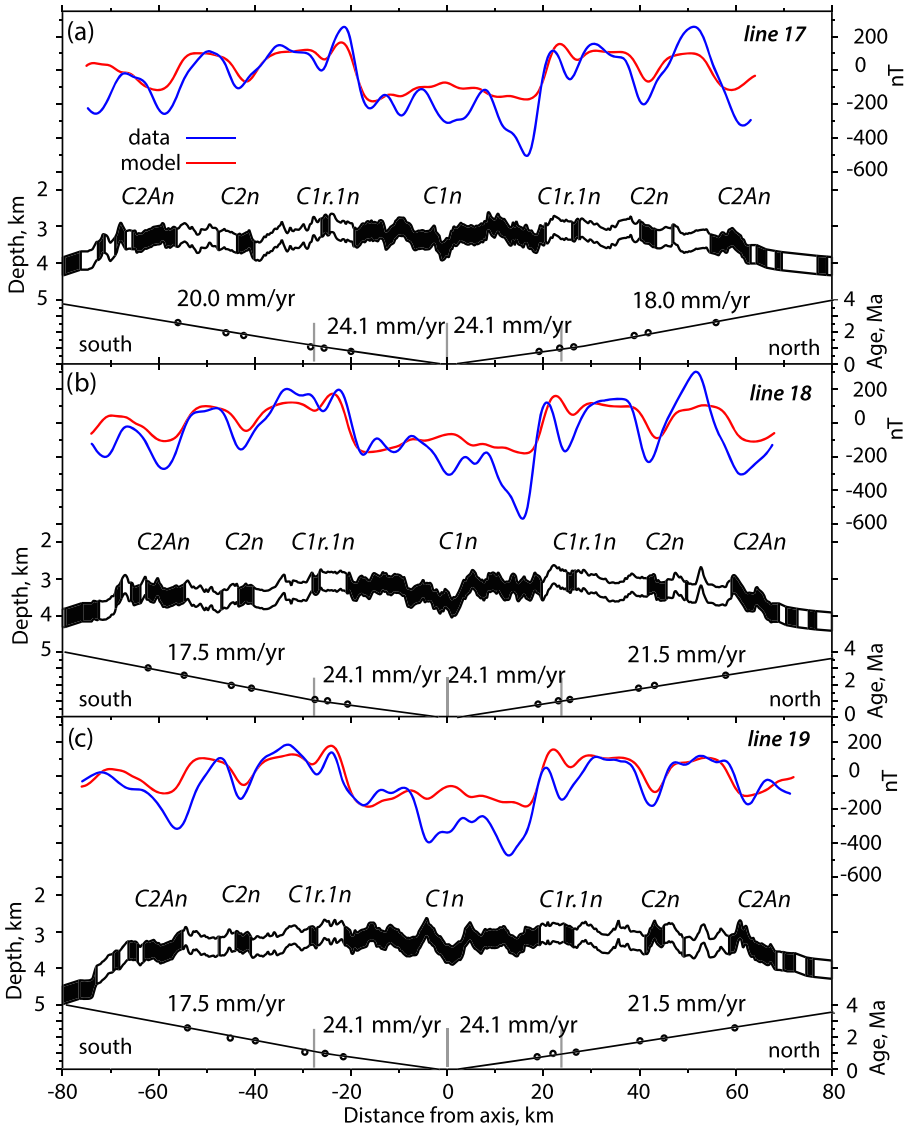

Figure 8. (a–c) Magnetic anomaly data and models for Lines 17–19 on Figure 3a. Blue/red lines: observed/modeled magnetic anomalies, respectively; black/white polygons: seafloor bathymetric profile and modeled magnetized blocks with labels for selected magnetic chrons (Ogg, 2012); solid black dots and lines: magnetic chron picks and age-distance fit, with half-spreading rates noted; vertical gray lines: changes in spreading rate.

configuration of the plate boundaries at the triple junction with the location of the probable Galapagos-Cocos-Nazca triple junction marked. As can be seen in Figure 1, opening of the first three segments at the western end of the Galapagos gore (s1–s3) occurs within the very slow spreading C-G regime. Using the rate of 48.2 mm/year obtained from this study for current C-N spreading, the opening rates estimated by Smith and Schouten (2018) for s1, s2, and s3 increase by ~20% but remain slow spreading at ~19, ~23, and ~29 mm/year, respectively.

6.1.1. Stages From Rifting to Spreading

The progression from Segments s1 to s3 documents the transition from initial rifting to magmatic seafloor spreading: Segment s1 is the newest rift basin, s2 is the transition segment, and all evidence suggests that s3 is spreading magmatically. The distribution of seismicity (Figure 2a) indicates that slip on the gore bounding faults at s3 is minor compared to s1 and s2. When magma is abundant, extension by dike intrusion is expected to accommodate the far-field extensional stress (e.g., Ebinger et al., 2013). Thus, the cessation of

widespread seismicity near the eastern end of s2 supports the idea that magmatic spreading begins at s3, with magmatism accommodating most of the extension.

The IRR detachment fault borders the axis of s2 on the north. Smith and Schouten (2018) conjectured that the formation of the detachment fault in s2 reflected the slowdown in spreading rate and presumed lower melt supply associated with C-G spreading. The IRR is the only detachment fault identified along the rift axis in the study area. An inspection of the available multibeam bathymetry data in the entire study area out to the gore scarps yields only one feature at the base of the scarps near 100°45′W that is similar in morphology to the IRR. As observed in other areas, however, without additional information other than the surface-collected bathymetry, it is difficult to identify this feature as a low-angle detachment fault or to rule out that other features are not detachments (e.g., Smith et al., 2014). From the presumed absence of detachments in the study area other than the IRR, however, it appears that the normal mode of C-N spreading development has not favored detachment fault formation during the transition to magmatic spreading.

It has been suggested that melt supply must fall within a certain range to form and maintain slip on low-angle detachment faults (e.g., Buck et al., 2005; Olive et al., 2010; Tucholke et al., 2008). If this is the case, then perhaps, magma supply reached the maximum threshold for detachment fault formation more quickly during the faster C-N opening than currently during slower C-G opening, and thus, the formation of large-offset detachment faults was inhibited. Since the present kinematic configuration is relatively new, more rift segments will need to form within the slow spreading C-G regime to determine if detachment fault formation will remain a stage in the transition to magmatic spreading.

6.1.2. Axial Morphology

The decrease in opening rate at 1.4 Ma from the C-N to C-G regime might also be reflected in a change in the morphology of the axial zone of magmatically spreading segments. The morphology of the ridge axes of Segments s4–s9, which open in the C-N spreading regime, is that of a shallow graben within which numerous small volcanoes have been constructed. This axial morphology is similar to that of three segments east of the study area between 98°W and the 95.5°W propagator (e.g., Detrick et al., 2002; Sinton et al., 2003), which are thought to be largely outside of the area influenced by the Galapagos hotspot (e.g., Canales et al., 2002; Sinton et al., 2003). We conclude that s4–s9 display the characteristic morphology of C-N spreading. (Note that close to the Galapagos hotspot the C-N spreading center is commonly referred to as the Galapagos spreading center.)

Once magmatic spreading is fully established at Segments s1–s3, the axial morphology may be different from that of s4–s9 and more similar to other slow spreading ridges, which typically have rift valleys. Currently, s2 has a rift valley. The AVR at the eastern section of s2 is similar in size to AVRs observed at the slow spreading (~25 mm/year) northern MAR (e.g., Searle et al., 2010). How will s2 evolve? Eruptions may fill the valley floor burying the AVR, and the IRR detachment fault may be abandoned. This might yield a morphology similar to segments to the east. Another possibility is that s2 will continue to display a rift valley with an AVR along the axis and perhaps a detachment fault on one side of the axis as commonly observed at the northern MAR (e.g., Escartín et al., 2008). At the estimated slow opening rate of 29 mm/year, s3 may also develop a rift valley as it continues to evolve.

6.2. Establishment of Magmatic Spreading

The history of the establishment of magmatic spreading is displayed along the length of the s2 transition segment. At the deep western end of s2, which is ~0.375 Ma younger than the eastern end, a hummocky seafloor hints that magmatism may be just emerging. In the older eastern half, magmatism is sufficient to create a large AVR. As magmatism is enhanced at s2, we assume that the AVR will continue to build toward the western end of the segment.

The AVR in s2 appears to be a continuation of a volcanic ridge in s3 that now borders the s3 axis on the north (Figure 4a). It is possible that at some point in the past, the volcanic ridge in s2 and s3 was a single AVR that extended across the two segments. South of the axis of s3, a large volcanic ridge links to a faulted volcanic ridge south of the axis of s4 in the same way that the AVR in s2 links to the volcanic ridge in s3 (Figure 4a). Similar to the s2 and s3 volcanic ridges, it is possible that a single AVR spanned s3 and s4. If this is the case, dikes from a magmatically spreading segment may propagate westward into the adjacent rift basin as part of the development of the magma supply system.

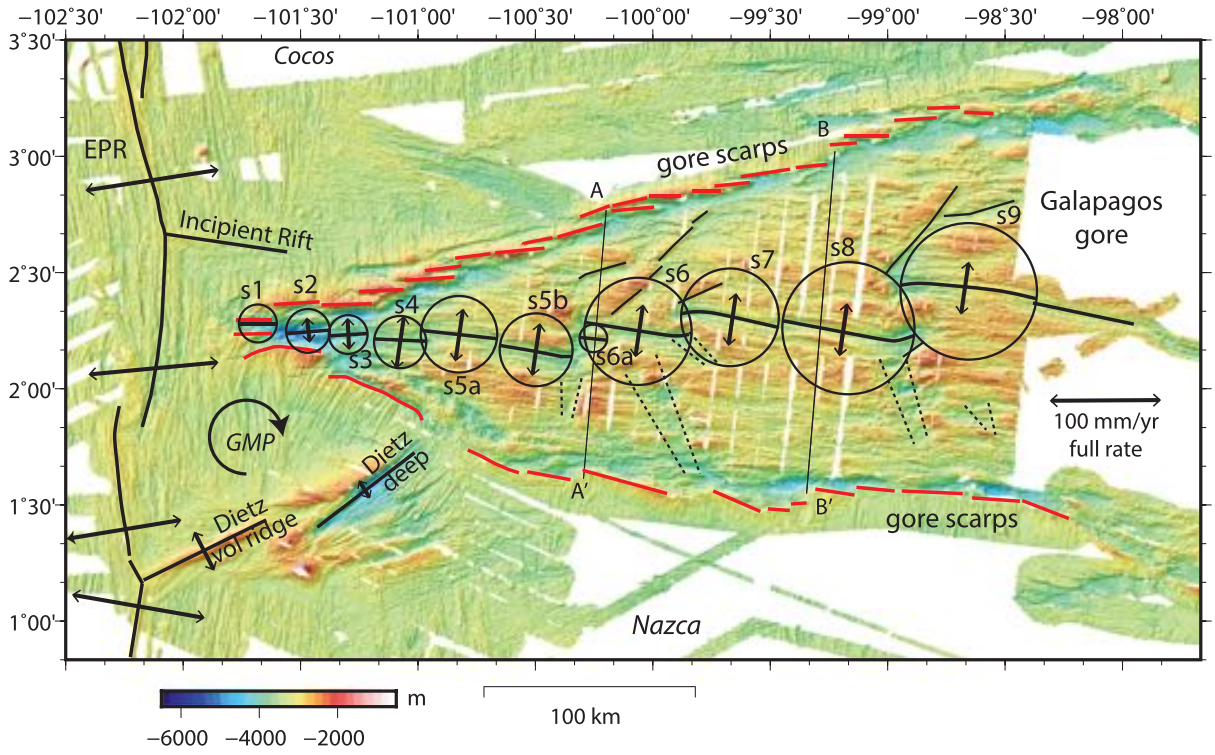

Figure 9. Bathymetry of the Galapagos triple junction region. Segments along the C-N gore are labeled. Circles are scaled to the length of the segment axis to aid in visualizing the variation in lengths. Traces of segment propagation are marked. Thin solid black lines: pseudofaults. Dashed black lines: regions transferred from one plate to the other and spread off-axis. Red lines: gore faults. The lengths of the northern gore faults are plotted in Figure 5a. Arrows: spreading directions from Figure 1. Arrows are scaled by spreading rate. Matching offsets in the northern and southern gore scarps are marked by A-A′ and B-B′ and corroborate a long-term C-N spreading direction of 007.

The western end of s3 is currently ~50 km from the actively propagating tip of the gore, and the western end of s2 is ~25 km from the tip. The gore tip is estimated to propagate westward at roughly half the EPR spreading rate (64 mm/year) (e.g., Lonsdale, 1988; Schouten et al., 2008). If magmatic spreading propagates at the same rate, in <0.5 Ma, full magmatic spreading will be established at s2, s1 will be a transition segment, and a new rift basin may have opened west of s1.

6.3. Development of Segmentation

Initial rift basins appear to achieve much of their length early in their formation. The lengths of s1–s4 do not vary substantially (17, 24, 18, and 24 km, respectively), and the lengths of gore bounding faults on the north side of the gore also fall within this range (Figure 5a). The initial lengths of rift basin scarps may be controlled by the strength of the lithosphere into which the rift tip propagates.

6.3.1. Westward Propagation of Individual Segments

Westward propagation of spreading segments is common in the study area beginning at Segment s6 and modifies the initial segmentation. Propagation is marked in the topography as V-shaped pseudofaults, failed rift basins, and oblique fabrics in the zone of lithosphere transferred from one plate to the other (Figure 9). As described by Hey et al. (1986), the receding rift fails and breaks into short sections as spreading slows and stops, and these short sections (basins) are carried off axis. The bathymetric continuity and linearity of large parts of the outer pseudofaults imply that propagation has been continuous at times (see outer pseudofault of s6 in Figure 9). The off-axis traces of propagation correspond to offsets in the magnetic lineations (Figure 3a) and highs in the MBA (Figure 3b).

Most outer pseudofaults begin several tens of km south of the northern gore wall, indicating that propagation begins ~1 Ma after rifting initiates. The outer pseudofault associated with the westward propagation of s6, however, initiates closer to the northern gore walls (~10 km from the gore scarps). If a

well-developed magma supply is necessary for propagation to begin, then magma supply to s6a must have been established quickly.

The azimuth of the outer pseudofaults of Segments 6a, 6, and 7 yields propagation rates ranging between 12 and 54 mm/year. The latter rate is similar to that estimated by Hey et al. (1986) for the 95.5°W propagator east of the study area. It appears that occasionally, the westward propagation of a segment stalls and the failing rift axis advances eastward a few tens of km. This may have occurred recently between s8 and s9 and would explain why the spalled off failed rift basins do not align with the eastern end of s8 (Figure 9).

6.3.2. Segment Lengths

There is a gradual increase in the length of spreading segments from ~20 km near the western tip of the gore to about 75 km at 350 km from the gore tip (Figures 5a and 9). In contrast, fault lengths bounding the gore on its north side do not increase with distance from the tip. Their lengths average 19 ± 4 km. Assuming that gore scarp lengths reflect the lengths of the initial rift basins/segments, the consistency of the fault lengths suggests that initial segment lengths have remained more or less constant for the last 5-6 My at ~20 km.

The mechanism for segment lengthening is not clear. Westward propagation of individual segments is common, but propagation both lengthens and shortens segments. Another idea is that segmentation wavelength, and thus segment length, is related to the development and enhancement of 3-D mantle upwelling. MBA values decrease and become more circular and centered within individual segments east of s6, supporting the notion of hotter temperatures and increasing mantle upwelling beneath these eastern segments.

It was suggested early on that the structure of 3-D mantle upwelling is controlled by melt diapirs rising from a buoyant, low-viscosity layer at depth (e.g., Crane, 1985; Whitehead et al., 1984) with increasing thickness of the layer, hotter temperature, and faster spreading rates leading to increased spacing of the diapirs. Many others have explored 3-D mantle upwelling beneath spreading centers since then (e.g., Carbotte et al., 2015; Choblet & Parmentier, 2001; Lin & Phipps Morgan, 1992; Rabinowicz & Briais, 2002). If segments in the study area lengthen in response to the development of mantle upwelling with a preferred spacing between melt diapirs, then the initial 20-km-long segments must merge or be subsumed by other segments. We examined the off-axis topography to investigate the evolution of segmentation. The results are inconclusive, however, because the topography is difficult to interpret (see off-axis bathymetry for s5a in Figure 4, for example). Magnetic anomalies also do not provide sufficient constraints because their continuity is based on widely spaced tracks. Whether final segment lengths in the study area will remain variable (i.e., 40–75 km) or possibly continue to evolve to reflect an evolving mantle upwelling structure or some other process remains unknown. East of the study area, segment lengths are variable and in the same range but become influenced by the Galapagos hot spot (Sinton et al., 2003).

6.3.3. Lengths and Styles of Lateral Offsets Between Segments

North-south lateral offset will increase if a propagating segment overtakes and eliminates the adjacent segment to the west. One example of a segment being eliminated is s6a whose westward propagation appears to have stalled. The rapid westward propagation of adjacent segment s6 has eliminated all but a small section of s6a. If s6 overtakes s6a, the resulting offset will be between s6 and s5b and will be ~18 km. The offset between s8 and s9 (~27 km, Figure 5b) would be the only one larger than this. Increasing north-south lateral offset also might be related to increasing segment length. In the study region, segment spreading direction is not orthogonal to the symmetry axis of the Galapagos gore (see Figure 5c, inset), and because of this longer segments will have larger offsets.

The contrasting styles of the observed offsets in the study area, which vary from simple with no defining topographic features between them to large, faulted, and rotated highs, are likely controlled by a combination of factors including the amount of offset, the trends of the segments, and the amount of overlap. Such factors influence the mechanical properties and ultimately the strength of the lithosphere within the offset. Where topographic highs are observed within offset zones, we expect that they reflect an increase in lithospheric age, and thus lithospheric strength, associated with larger lateral offsets.

7. Conclusions

Bathymetry, magnetic, and gravity data collected over the first nine segments in the western section of the Galapagos gore are used to examine how individual magmatic spreading segments are established and evolve. The transition from rifting to magmatic spreading presently occurs over the three westernmost

segments (s1, s2, and s3) all within the very slow spreading C-G spreading regime. Segments s4–s9 originated within the intermediate-spreading C-N regime.

Segment s2 marks the transition between rifting and full magmatic spreading. At its deep western end, which is roughly 0.375 Ma younger than the eastern end, hummocky seafloor suggests that magmatism may be just emerging. At its older eastern end, the magmatism is sufficient to create a well-developed AVR. We assume the AVR will continue to build westward as magma supply is enhanced.

The only detachment fault identified in the survey area is at Segment s2 where the active IRR detachment borders the axis at the base of the northern gore scarp. Melt supply along s2 must be within the range for oceanic detachment fault formation (e.g., Buck et al., 2005; Olive et al., 2010; Tucholke et al., 2008; Whitney et al., 2013). Because detachment faults are apparently absent elsewhere along the gore scarps, melt supply to Segments s4–s9 during initial rifting may have reached the maximum threshold for detachment fault formation faster than at the current transition segment, s2.

Magnetic anomalies and regular, lineated abyssal hill topography show that seafloor spreading has been well organized along Segments s4–s9 and suggests that magmatic spreading developed quickly. The only features that disturb the anomalies are a result of the westward propagation of segments. A change in Cocos-Nazca spreading rate from 39 to 48.2 mm/year is documented at ~1.1 Ma. The spreading direction in the study area has remained unchanged at 007.

MBA values decrease to the east along the axis. The first occurrence of a (somewhat diffuse) MBA low centered on the axis is ~180 km from the gore tip. The MBA low becomes more circular and centered within individual segments farther east, suggesting increasing temperatures and mantle upwelling, and perhaps progression to a developed melt supply.

At the western tip of the Galapagos gore the lengths of newly formed segments have averaged ~20 km for the last 5–6 My based on the lengths of the northern gore wall faults. These segment lengths are likely controlled by the strength of the lithosphere at the gore tip. Segment lengths increase with increasing distance from the tip. The eventual spacing of segments may be related to the structure of the developing 3-D mantle upwelling and the spacing between upwelling centers.

Data Availability Statement

Multibeam bathymetry, magnetic, and gravity data access is through the Rolling Deck to Repository website (https://www.rvdata.us/search/cruise/SR1806); bathymetry from the broader region can be obtained from the Marine Geoscience Data System website (http://www.marine-geo.org/index.php). T-phase origins are available online (from http://www.pmel.noaa.gov/acoustics/). Focal mechanisms for teleseismically recorded earthquakes are available from the Centroid Moment Tensor catalog (http://www.globalcmt.org/CMTsearch.html). Bathymetry data are displayed using Generic Mapping Tools software (Wessel & Smith, 1991).

Acknowledgments

E. M. and H. S. are grateful to the National Science Foundation for funding this work and to InterRidge and the University of Leeds for providing support for a number of the international students and scholars who were able to participate on the cruise. We are also grateful for the extraordinary work of the Captain and crew of R/V *Sally Ride*, whose efficiency and good cheer made the cruise such a success. We thank M. Ligi and two anonymous reviewers for their comments which greatly improved the manuscript. Any opinion, findings, and conclusions or recommendations expressed in this material are those of the authors and do not necessarily reflect the views of the National Science Foundation.

References

Ballu, V., Hildebrand, J. A., & Canuteson, E. L. (1999). The density structure associated with oceanic crutal rifting at the Hess deep: A seafloor and sea-surface gravity study. *Earth and Planetary Science Letters*, *171*(1), 21–34. https://doi.org/10.1016/S0012-821X(99)00132-6

Buck, W. R., Lavier, L. L., & Poliakov, A. N. B. (2005). Modes of faulting at mid-ocean ridges. *Nature*, *434*(7034), 719–723. https://doi.org/10.1038/nature03358

Canales, J. P., Ito, G., Detrick, R. S., & Sinton, J. M. (2002). Crustal thickness along the western Galápagos spreading center and the compensation of the Galápagos hotspot swell. *Earth and Planetary Science Letters*, *203*(1), 311–327. https://doi.org/10.1016/S0012-821X(02)00843-9

Carbotte, S. M., Smith, D. K., Cannat, M., Klein, E. M., Wrigth, T. J., Ayele, A., et al. (Eds.). (2015). Tectonic and magmatic segmentation of the global ocean ridge system: A synthesis of observations. *Magmatic rifting and Active Volcanism* (Vol. *420*). London: The Geological Society of London. https://doi.org/10.1144/SP420.5

Caress, D. W., & Chayes, D. N. (1996). Improved processing of Hydrosweep DS multibeam data on the R/V Maurice Ewing. *Marine Geophysical Researches*, *18*(6), 631–650. https://doi.org/10.1007/BF00313878

Choblet, G., & Parmentier, E. M. (2001). Mantle upwelling and melting beneath slow-spreading ridge centers: Effects of variable rheology and melt productivity. *Earth and Planetary Science Letters*, *184*(3-4), 589–604. https://doi.org/10.1016/S0012-821X(00)00330-7

Crane, K. (1985). The spacing of ridge-axis highs: Dependence upon diapiric processes in the underlying asthenosphere? *Earth and Planetary Science Letters*, *72*, 405–414. https://doi.org/10.1016/0012-821x(85)90061-5

DeMets, C., Gordon, R. G., & Argus, D. F. (2010). Geologically current plate motions. *Geophysical Journal International*, *181*(1), 1–80. https://doi.org/10.1111/j.1365-246X.2009.04491.x

DeMets, C., Gordon, R. G., Argus, D. F., & Stein, S. (1994). Effect of recent revisions to the geomagnetic reversal time scale on estimates of current plate motions. *Geophysical Research Letters*, *21*(20), 2191–2194. https://doi.org/10.1029/94GL02118

DeMets, C., & Wilson, D. S. (2008). Toward a minimum change model for recent plate motions: Calibrating seafloor spreading rates for outward displacement. *Geophysical Journal International*, *174*(3), 825–841. https://doi.org/10.1111/j.1365-246X.2008.03836.x

Detrick, R. S., Sinton, J. M., Ito, G., Canales, J. P., Behn, M. D., Blacic, T., et al. (2002). Correlated geophysical, geochemical, and volcanological manifestations of plume-ridge interaction along the Galápagos Spreading Center. *Geochemistry, Geophysics, Geosystems*, *3*(10), 8501. https://doi.org/10.1029/2002GC000350

Ebinger, C. J., van Wijk, J., & Keir, D. (2013). The time scales of continental rifting: Implications for global processes. In M. W. Bickford (Ed.), *The Web of Geological Sciences: Advances, Impacts, and Interactions* (Vol. 500, pp. 1–26). Geological Society of America Special Paper. https://doi.org/10.1130/2013.2500(11)

Ekström, G., Nettles, M., & Dziewonski, A. M. (2012). The global CMT project 2004-2010: Centroid-moment tensors for 13,017 earthquakes. *Physics of the Earth and Planetary Interiors*, *200-201*, 1–9. https://doi.org/10.1016/j.pepi.2012.1004.1002

Escartín, J., Smith, D. K., Cann, J., Schouten, H., Langmuir, C. H., & Escrig, S. (2008). Central role of detachment faults in accretion of slow-spread oceanic lithosphere. *Nature*, *455*, 790–794. https://doi.org/10.1038/nature07333

Ferrini, V. L., Shillington, D. J., Gillis, K., MacLeod, C. J., Teagle, D. A. H., Morris, A., et al. (2013). Evidence of mass failure in the Hess Deep Rift from multi-resolutional bathymetry data. *Marine Geology*, *339*, 13–21. https://doi.org/10.1016/j.margeo.2013.03.006 www.sciencedirect.com/science/article/pii/S0025322713000364

Fox, C. G., Matsumoto, H., & Lau, T.-K. (2001). Monitoring Pacific Ocean seismicity from an autonomous hydrophone array. *Journal of Geophysical Research*, *106*(B3), 4183–4206. https://doi.org/10.1029/2000JB900404

Francheteau, J., Armijo, R., Cheminee, J. L., Hekinian, R., Lonsdale, P., & Blum, N. (1990). 1 ma East Pacific rise oceanic crust and uppermost mantle exposed by rifting in Hess deep (equatorial Pacific Ocean). *Earth and Planetary Science Letters*, *101*(2-4), 281–295. https://doi.org/10.1016/0012-821X(90)90160-Y

Gillis, K. M., Mevel, C., & Allan, J. F. (1993). *Proc. ODP, Init. Repts* (Vol. 147). College Station, TX: Ocean Drilling Program. https://doi.org/10.2973/odp.proc.ir.147.1993

Gillis, K. M., Snow, J. E., Klaus, A., Abe, N., Adriao, A. B., Akizawa, N., et al. (2014). Primitive layered gabbros from fast-spreading lower oceanic crust. *Nature*, *505*(7482), 204–207. Letter. https://doi.org/10.1038/nature12778

Hey, R. (1977). Tectonic evolution of the Cocos-Nazca spreading center. *Geological Society of America Bulletin*, *88*(10), 1404–1420. https://doi.org/10.1130/0016-7606(1977)88%31404:TEOTCS%3E2.0.CO;2

Hey, R. N., Kleinrock, M. C., Miller, S. P., Atwater, T. M., & Searle, R. C. (1986). Sea Beam/Deep-Tow investigation of an active oceanic propagating rift system, Galapagos 95.5°W. *Journal of Geophysical Research*, *91*(B3), 3369–3393. https://doi.org/10.1029/JB091iB03p03369

Hill, E. J., Baldwin, S. L., & Lister, G. S. (1995). Magmatism as an essential driving force for formation of active metamorphic core complexes in eastern Papua New Guinea. *Journal of Geophysical Research*, *100*, 10,441–10,451. https://doi.org/10.1029/94JB03329

Holden, J. C., & Dietz, R. S. (1972). Galapagos Gore, NazCoPac triple junction and Carnegie/Cocos ridges. *Nature*, *235*(5336), 266–269. https://doi.org/10.1038/235266a0

IAGA (2010). Internation Geomagnetic Reference field: The elevent generation, International Association of Geomagnetism and Aeronomy, Working Group V-MOD. *Geophysical Journal International*, *183*, 1216–1230. https://doi.org/10.1111/j.1365-246X.2010.04804.x

Karson, J. A., Klein, E., Hurst, S., Lee, C., Rivizzigno, P., Curewitz, D., et al. (2002). Structure of the uppermost fast-spread oceanic crust exposed at the Hess Deep Rift: Implications for subaxial processes at the East Pacific Rise. *Geochemistry, Geophysics, Geosystems*, *3*(1), https://doi.org/10.1029/2001GC000155

Klein, E. M., Smith, D. K., Williams, C. M., & Schouten, H. (2005). Counter-rotating microplates at the Galapagos triple junction, eastern equatorial Pacific Ocean. *Nature*, *433*(7028), 855–858. https://doi.org/10.1038/nature03262

Kuo, B. Y., & Forsyth, D. W. (1988). Gravity anomalies of the ridge-transform system in the South Atlantic between 31° and 34.5°S: Upwelling centers and variations in crustal thickness. *Marine Geophysical Researches*, *10*(3-4), 205–232. https://doi.org/10.1007/BF00310065

Lin, J., & Phipps Morgan, J. (1992). The spreading rate dependence of three-dimensional mid-ocean ridge gravity structure. *Geophysical Research Letters*, *19*(1), 13–16. https://doi.org/10.1029/91GL03041

Lin, J., Purdy, G. M., Schouten, H., Sempere, J. C., & Zervas, C. (1990). Evidence from gravity data for focused magmatic accretion along the mid-Atlantic ridge. *Nature*, *344*(6267), 627–632. https://doi.org/10.1038/344627a0

Little, T. A., Baldwin, S. L., Fitzgerald, P. G., & Monteleone, B. (2007). Continental rifting and metamorphic core complex formation ahead of the woodlark spreading ridge, D'Entrecasteaux Islands, Papua New Guinea. *Tectonics*, *26*, TC1002. https://doi.org/10.1029/2005TC001911

Lonsdale, P. (1977). Regional shape and tectonics of the equatorial East Pacific rise. *Marine Geophysical Researches*, *3*(3), 295–315. https://doi.org/10.1007/BF00285657

Lonsdale, P. (1988). Structural patterns of the Galapagos microplate and evolution of the Galapagos triple junction. *Journal of Geophysical Research*, *93*(B11), 13,551–13,574. https://doi.org/10.1029/JB093iB11p13551

Lonsdale, P., Blum, N., & Puchelt, H. (1992). The RRR triple junction at the southern end of the Pacific-Cocos East Pacific rise. *Earth and Planetary Science Letters*, *109*(1-2), 73–85. https://doi.org/10.1016/0012-821X(92)90075-7

MacLeod, C. J., Früh-Green, G. L., & Manning, C. E. (1996). Tectonics of Hess deep: A synthesis of drilling results from leg 147. In C. Mével, K. M. Gillis, J. F. Allan, & P. S. Meyer (Eds.), *Proc. of the Ocean Drilling Program Sci. Res* (Vol. 147, pp. 461–475). College Station, TX: Ocean drilling program.

Martínez, F., Taylor, B., & Goodlife, A. M. (2001). Metamorphic core complex formation by density inversion and lower-crust extension. *Nature*, *411*(6840), 930–934. https://doi.org/10.1038/35082042

Mendel, V., Munschy, M., & Sauter, D. (2005). MODMAG, a MATLAB program to model marine magnetic anomalies. *Computers & Geosciences*, *31*(5), 589–597. http://www.sciencedirect.com/science/article/pii/S0098300404002316. https://doi.org/10.1016/j.cageo.2004.11.007

Ogg, J. G. (2012). Geomagnetic polarity time scale. In F. M. Gradstein, J. G. Ogg, M. Schmidtz, & G. Ogg (Eds.), *The geologic time scale* (Chap. 5, pp. 85–113). Amersterdam: Elsevier. https://doi.org/10.1016/B978-0-444-59425-9.00005-6

Olive, J.-A., Behn, M. D., & Tucholke, B. E. (2010). The structure of oceanic core complexes controlled by the depth distribution of magma emplacement. *Nature Geoscience*, *6*(9), 755–760. https://doi.org/10.1038/NGEO1888

Parker, R. L. (1972). The rapid calculation of potential anomalies. *Geophysical Journal of the Royal Astronomical Society*, *31*, 447–455. https://doi.org/10.1111/j.1365-246x.1973.tb06513.x

Rabinowicz, M., & Briais, A. (2002). Temporal variations of the segmentation of slow to intermediate spreading mid-ocean ridges. 2. A three-dimensional model in terms of lithospheric accretion and convection within the partially molten mantle. *Journal of Geophysical Research*, *107*(B6), 2098. https://doi.org/10.1029/2001JB000343

Schouten, H., Smith, D. K., Montési, L., Zhu, W., & Klein, E. M. (2008). Unstable northern rifts of the Galapagos Triple Junction, Eastern Equatorial Pacific. *Geology*, *36*, 339–342. https://doi.org/10.1130/G24431A.24431

Searle, R. C. (1989). Location and segmentation of the Cocos-Nazca spreading Centre west of 95° W. *Marine Geophysical Researches*, *11*(1), 15–26. https://doi.org/10.1007/BF00286245

Searle, R. C., & Francheteau, J. (1986). Morphology and tectonics of the Galapagos triple junction. *Marine Geophysical Researches*, *8*, 95–129.

Searle, R. C., Murton, B. J., Achenbach, K., LeBas, T., Tivey, M., Yeo, I., et al. (2010). Structure and development of an axial volcanic ridge: Mid-Atlantic ridge, 45°N. *Earth and Planetary Science Letters*, *299*(1–2), 228–241. http://www.sciencedirect.com/science/article/pii/S0012821X10005649. https://doi.org/10.1016/j.epsl.2010.09.003

Sinton, J. M., Detrick, R., Canales, J. P., Ito, G., & Behn, M. D. (2003). Morphology and segmentation of the western Galápagos Spreading Center, 90.5°–98°W: Plume-ridge interaction at an intermediate spreading ridge. *Geochemistry, Geophysics, Geosystems*, *4*(12), 8515. https://doi.org/10.1029/2003GC000609

Smith, D. K., & Schouten, H. (2018). Opening of Hess deep rift at the Galapagos triple junction. *Geophysical Research Letters*, *45*, 3942–3950. https://doi.org/10.1029/2018GL077555

Smith, D. K., Schouten, H., Dick, H. J. B., Cann, J. R., Salters, V., Marschall, H. R., et al. (2014). Development and evolution of detachment faulting along 50 km of the Mid-Atlantic Ridge near 16.5°N. *Geochemistry, Geophysics, Geosystems*, *15*, 4692–4711. https://doi.org/10.1002/2014GC005563

Smith, D. K., Schouten, H., Montési, L., & Zhu, W. (2013). The recent history of the Galapagos triple junction preserved on the Pacific plate. *Earth and Planetary Science Letters*, *371-372*, 6–15. https://doi.org/10.1016/j.epsl.2013.1004.1018

Smith, D. K., Schouten, H., Zhu, W., Montési, L., & Cann, J. R. (2011). Distributed deformation ahead of the Cocos-Nazca rift at the Galapagos triple junction. *Geochemistry, Geophysics, Geosystems*, *12*, Q11003. https://doi.org/10.1029/2011GC003689

Stewart, M. A., Klein, E. M., Karson, J. A., & Brophy, J. A. (2003). Geochemical relationships between dikes and lavas at the Hess Deep rift: Implications for magma eruptibility. *Journal of Geophysical Research*, *108*(B4), 2184. https://doi.org/10.1029/2001JB001622

Taylor, B., Goodliffe, A. M., & Martinez, F. (1999). How continents break up: Insights from Papua New Guinea. *Journal of Geophysical Research*, *104*(B4), 7497–7512. https://doi.org/10.1029/1998JB900115

Tisseau, J., & Patriat, P. (1981). Identification des anomalies magnétiques sur les dorsales à faible taux d'expansion: Méthode des taux fictifs. *Earth and Planetary Science Letters*, *52*(2), 381–396. https://doi.org/10.1016/0012-821x(81)90191-6 http://www.sciencedirect.com/science/article/pii/0012821X81901916

Tucholke, B. E., Behn, M. D., Buck, W. R., & Lin, J. (2008). Role of melt supply in oceanic detachment faulting and formation of mega-mullions. *Geology*, *36*, 455–458. https://doi.org/10.1130/G24639A.24631

Wessel, P., & Smith, W. H. F. (1991). Free software helps map and display data. *Eos, Transactions American Geophysical Union*, *72*(41), 441. https://doi.org/10.1029/90EO00319

Whitehead, J. A., Dick, H. J. B., & Schouten, H. (1984). A mechanism for magmatic accretion under spreading centers. *Nature*, *312*(5990), 146–148. https://doi.org/10.1038/312146a0

Whitney, D. L., Teyssier, C., Rey, P., & Buck, W. R. (2013). Continental and oceanic core complexes. *Geological Society of America Bulletin*, *125*(3–4), 273–298. http://gsabulletin.gsapubs.org/content/125/3-4/273.abstract, https://doi.org/10.1130/B30754.1

Wiggins, S. M., Dorman, L. M., Cornuelle, B. D., & Hildebrand, J. A. (1996). Hess Deep rift valley structure from seismic tomography. *Journal of Geophysical Research*, *101*(B10), 22,335–22,353. https://doi.org/10.1029/96JB01230

Wilson, D. S., & Hey, R. N. (1995). History of rift propagation and magnetization intensity for the Cocos-Nazca spreading center. *Journal of Geophysical Research*, *100*(B6), 10,041–10,056. https://doi.org/10.1029/95JB00762